

# Nerve Growth Factor-Targeted Molecular Theranostics Based on Molybdenum Disulfide Nanosheet-Coated Gold Nanorods (MoS<sub>2</sub>-AuNR) for Osteoarthritis Pain

Man Ting Au,<sup>§</sup> Jingyu Shi,<sup>§</sup> Yadi Fan, Junguo Ni, Chunyi Wen,<sup>\*</sup> and Mo Yang<sup>\*</sup>



Cite This: <https://doi.org/10.1021/acsnano.1c02454>



Read Online

ACCESS |



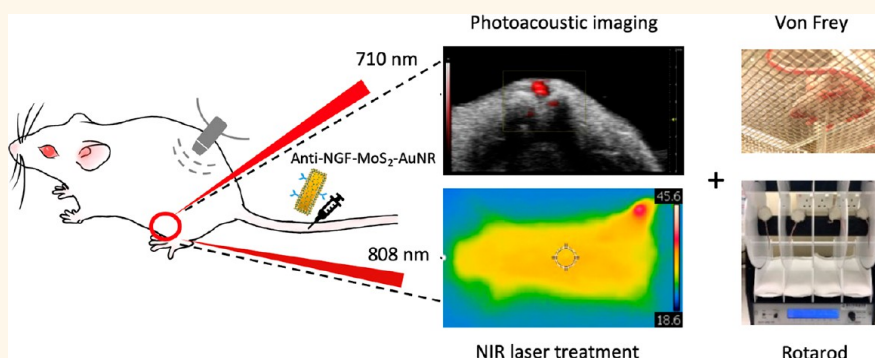
Metrics & More



Article Recommendations



Supporting Information



**ABSTRACT:** Osteoarthritis (OA) is a leading cause of chronic pain in the elderly worldwide. Yet current diagnosis and therapy for OA pain are subjective and nonspecific with significant adverse effects. Here, we introduced a theranostic nanoprobe based on molybdenum disulfide nanosheet-coated gold nanorods (MoS<sub>2</sub>-AuNR) targeting nerve growth factor (NGF), a key player in pain sensation, for photoacoustic pain imaging and near-infrared (NIR) imaging-guided photothermal analgesic therapy. MoS<sub>2</sub> coating significantly improved the photoacoustic and photothermal performance of AuNR. Functionalization of MoS<sub>2</sub>-AuNR nanoprobe by conjugating with NGF antibody enabled active targeting on painful OA knees in a surgical OA murine model. We observed that our functional nanoprobe accumulated in the OA knee rather than the contralateral intact one, and the amount was correlated with the severity of mechanical allodynia in our mouse model. Under imaging guidance, NIR-excited photothermal therapy could mitigate mechanical allodynia and walking imbalance behavior for both subacute and chronic stages of OA in a preclinical setting. This molecular theranostic approach enabled us to specifically localize the source of OA pain and efficiently block peripheral pain transmission.

**KEYWORDS:** molybdenum disulfide, gold nanorods, osteoarthritis, nerve growth factor, theranostics, pain relief

Osteoarthritis (OA) represents one of the most common painful conditions in the life of a human. It has caused a heavy healthcare and socioeconomic burden.<sup>1</sup> The pathophysiology of OA pain is a mixed picture involving both nociceptive and neuropathic mechanisms at both the peripheral and central level.<sup>2</sup> As a result, OA pain exhibits heterogeneous clinical presentations, which poses a huge challenge for clinical diagnosis and management.<sup>3</sup>

The current diagnosis of OA pain relies on the patients' subjective description and semiquantification *via* a visual analogue score, while the analgesic approaches are very limited such as nonspecific pain relief using nonsteroidal anti-

inflammatory drugs (NSAIDs) with significant systemic adverse effects after long-term use.<sup>4</sup> With the advancement of imaging technologies, functional magnetic resonance imaging, *i.e.*, blood oxygenation level-dependent imaging, has

**Received:** March 22, 2021

**Accepted:** June 28, 2021

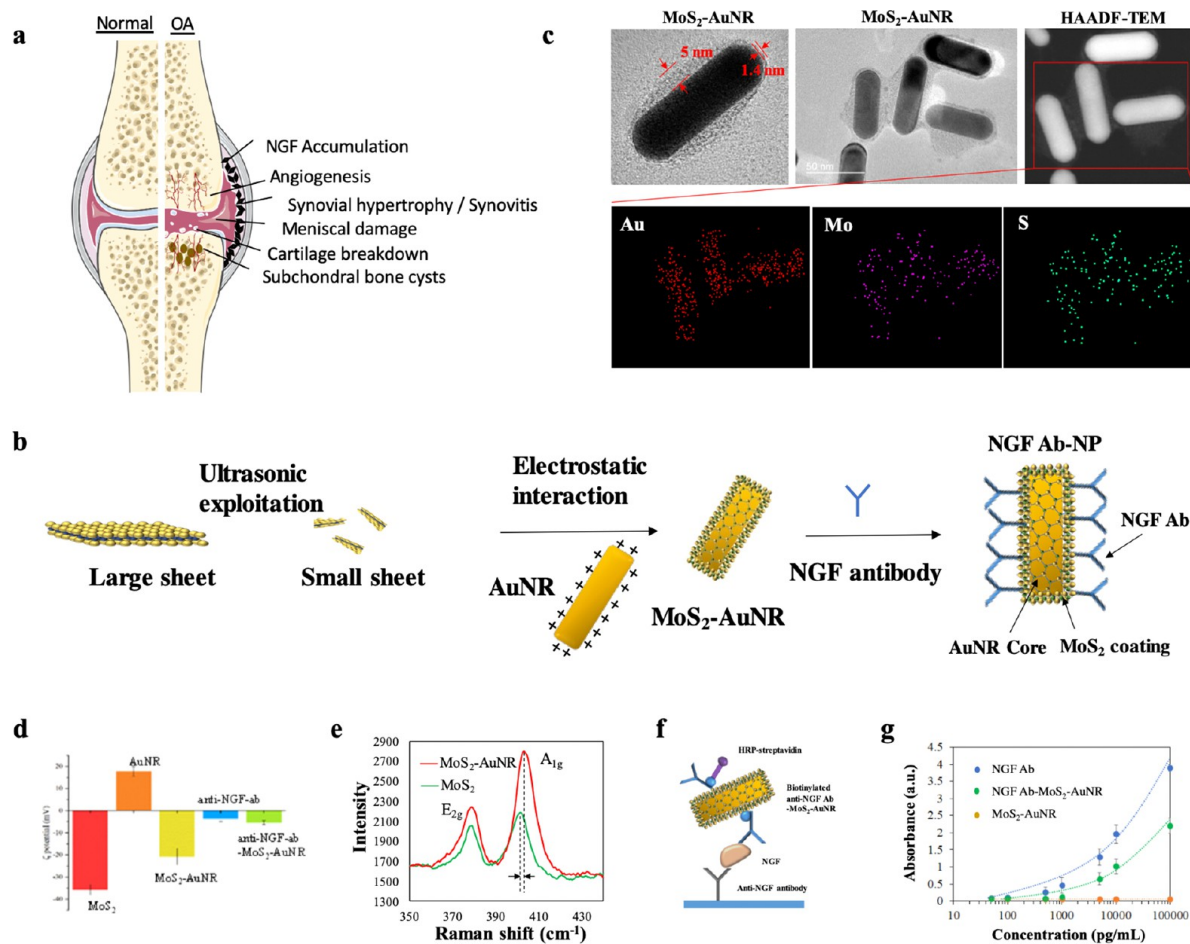


**Figure 1.** Theranostic platform for pain imaging in knee osteoarthritis. (a) Schematic diagram showing comparisons between normal and OA knee joints. (b) Positively charged CTAB-AuNR interacts with a negatively charged small  $\text{MoS}_2$  nanosheet *via* electrostatic interaction to obtain  $\text{MoS}_2$ -nanosheet-encapsulated AuNRs ( $\text{MoS}_2$ -AuNR). Then anti-NGF antibody binds to  $\text{MoS}_2$ -AuNRs *via* a covalent interaction between the  $\text{MoS}_2$  nanosheet with sulfur vacancies and free sulfhydryl groups of the antibody. Finally, an anti-NGF- $\text{MoS}_2$ -AuNRs nanocomplex was obtained. (c) HR-TEM images of single, multiple, and element mapping images of  $\text{MoS}_2$ -AuNR. (d) Zeta-potential of elements in anti-NGF- $\text{MoS}_2$ -AuNR, showing successful attachment of NGF antibody on  $\text{MoS}_2$ -AuNR. (e) Raman spectroscopy diagram of  $\text{MoS}_2$ -AuNR. (f, g) Binding affinity between the anti-NGF- $\text{MoS}_2$ -AuNR nanocomplex and NGF was assessed by (f) sandwich ELISA. (g) The absorbance at 450 nm was plotted against the increasing concentration of the antibody alone,  $\text{MoS}_2$ -AuNR alone, and the nanocomplex.

already enabled us to quantitatively investigate central pain sensitization components in OA pathophysiology.<sup>5,6</sup> However, it remains puzzling why patients with relatively less severe radiographic joint damage preoperatively experience much more pain after total joint replacement surgery,<sup>7</sup> and joint pain persistently occurs in around 10–20% of OA patients postsurgery.<sup>8</sup> Given the fact of the discordance between radiographic and symptomatic OA,<sup>9,10</sup> it prompts a huge unmet need for the development of imaging-based evaluation tools to precisely localize and quantify the peripheral OA pain generator, which will potentially lead to a paradigm shift in current analgesic and surgical practice.<sup>11</sup>

Activation and sensitization of peripheral afferent nerve fibers is the key step in OA pain generation and transmission.<sup>12</sup> Mounting evidence suggests that nerve growth factor (NGF), a crucial protein in the development and survival of neurons,<sup>13</sup> plays a pivotal role in peripheral nerve activation and sensitization.<sup>14,15</sup> In response to mechanical or inflammatory stimuli, articular chondrocytes and synovial fibroblasts secrete NGF *in vitro*, which would trigger pain sensation in an OA joint.<sup>16,17</sup> Accumulation of NGF could also be observed in

humans and animal models *in vivo*.<sup>16,18,19</sup> In a well-received posttraumatic OA mouse model induced by surgical destabilization of medial meniscus (DMM), the level of NGF mRNA in arthritic joint tissues reached a peak in the first week and at 4 months after surgery,<sup>15</sup> while the synovial NGF protein level also significantly increased at 4 weeks postsurgery.<sup>20</sup> It has been known that the binding of NGF to its receptor, tropomyosin receptor kinase A (TrkA), leads to a rapid potentiation of transient receptor potential cation channel, subfamily V, member 1 (TRPV1) and triggers pain sensitization in primary afferent sensory neurons.<sup>21</sup> NGF also contributes to pain hypersensitivity in the arthritic joint.<sup>22,23</sup> Intra-articular injection of NGF increased the sensitivity of OA knees to pain stimuli.<sup>17</sup> Blockade of NGF signaling *via* either a soluble recombinant form of NGF receptor or a selective TrkA inhibitor could effectively suppress the pain in various animal models of OA.<sup>15,24</sup> It is very exciting that NGF neutralizing antibody is an emerging analgesic therapy for OA now in phase III clinical trials.<sup>25</sup> In recent years, there is increasing use of nanoprobes (cationic nanoprobes) and biomarkers (inflammatory and noninflammatory cytokines) in OA theranostics.<sup>26–28</sup>

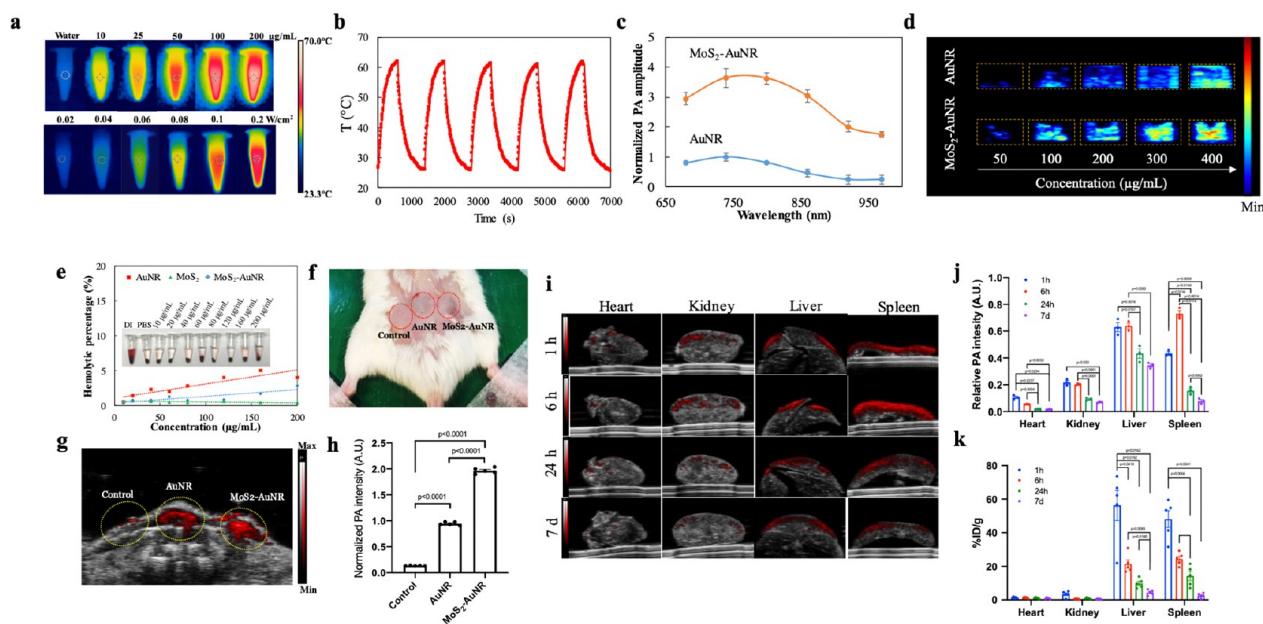


**Figure 2.** Characterization and biocompatibility of MoS<sub>2</sub>-AuNR. (a) Thermal images of MoS<sub>2</sub>-AuNR with increasing concentration (upper row) and increasing laser power (lower row) at 200 µg/mL. (b) Photothermal stability study of MoS<sub>2</sub>-AuNR (200 µg/mL) under photothermal heating and natural cooling cycles. (c) Normalized PA amplitude of AuNR and MoS<sub>2</sub>-AuNR under different wavelengths. (d) PA signals for AuNRs and MoS<sub>2</sub>-AuNR showed a dose-dependent increase at 710 nm. (e) Percentages of hemolysis induced by AuNRs, MoS<sub>2</sub>, and MoS<sub>2</sub>-AuNR at various concentrations. Inset image shows the direct observation of hemolysis by MoS<sub>2</sub>-AuNR. (f) Subcutaneous injection of control (Matrigel), AuNRs, and MoS<sub>2</sub>-AuNR into a mouse in prone position (*n* = 5). (g) US-PA overlay image obtained by *in vivo* PA imaging using an LZ250 transducer at 710 nm. (h) Quantitative analysis of PA signals from (g) showing an enhanced signal with MoS<sub>2</sub>-AuNR. (i) US-PA overlay images showing PA signals at 710 nm of *ex vivo* organs and tissues (heart, kidney, liver, and spleen) from mice at 1 h, 6 h, 24 h, and 7 days post-*i.v.* injection of MoS<sub>2</sub>-AuNR (*n* = 3 each group). (j) Semiquantitative biodistribution of MoS<sub>2</sub>-AuNR in mice determined by the average PA intensity of major organs. (k) ICP-MS analysis reflecting the amount of gold element in MoS<sub>2</sub>-AuNR in the excised tissues. A single intravenous injection of 3.5 mg/kg MoS<sub>2</sub>-AuNR was given to the mice (*n* = 20, 5 per group). Organs were collected after 1 h, 6 h, 24 h, or 7 days of injection. Statistical analyses were performed using ordinary one-way ANOVA with Tukey's *posthoc* test.

Therefore, NGF-targeted molecular imaging using nanoprobe for OA pain will enable us to better understand the origin of OA pain toward personalized analgesic therapy.

Photoacoustic (PA) imaging is a noninvasive hybrid imaging modality, which has rapidly aroused great attention as a diagnostic tool with a nonionizing property, high spatial resolution, and deep penetration depth compared with optical imaging.<sup>29</sup> Plasmonic nanoparticles such as gold nanostructures (10–200 nm) have been extensively studied as PA contrast imaging agents and photothermal transduction agents due to their great optical properties and easy biofunctionalization.<sup>30,31</sup> Compared with round gold nanoparticles (AuNPs) with main optical absorption in the visible light, anisotropic gold nanorods (AuNRs) are of higher interest for near-infrared (NIR)-excited PA imaging with the advantages of easy synthesis, tunable absorbance spectrum, and high absorption cross-section in the NIR region from 650 to 900 nm.<sup>32</sup> However, the poor photothermal stability of AuNRs limits their biomedical applications.<sup>33</sup> To improve the photothermal stability and enhance the PA imaging signal of AuNR, nanomaterials such as silica and reduced graphene oxide (rGO) with efficient thermal conductivity have been deployed to modify the AuNR surface to increase its photothermal stability.<sup>32,33</sup> However, silica has no photothermal absorption in the NIR region, which cannot enhance the photothermal performance of AuNRs.<sup>32</sup> The rGO coating with high NIR light absorption could enhance the photothermal performance of the AuNRs. But the hydrophobic property of rGO leads to

poor water dispersibility of the formed rGO-AuNR, which may hamper its biological applications.<sup>33</sup> Recently, other two-dimensional (2D) nanomaterials with graphene-like atomic planar structures have attracted more attention.<sup>34</sup> Among them, molybdenum disulfide (MoS<sub>2</sub>) is of the highest interest due to its great stability, easy synthesis, and unique chemical, electronic, and optical properties.<sup>35</sup> Especially, MoS<sub>2</sub> shows excellent biocompatibility and low cytotoxicity, which makes it suitable for biomedical applications.<sup>36–38</sup> Moreover, due to its high NIR absorbance and strongly negative surface charge, chemically exploited 2D MoS<sub>2</sub> nanosheets exhibit a good NIR heating feature as well as good water dispersibility.<sup>39</sup> Such properties of MoS<sub>2</sub> potentiate it as a superior contrast agent for PA imaging<sup>40</sup> or hybridization with the other nanomaterials for theranostic purposes.<sup>41,42</sup>

Here, we designed an NGF-targeting PA molecular theranostic nanoprobe based on 2D MoS<sub>2</sub> nanosheets-coated gold nanorods (MoS<sub>2</sub>-AuNR) for peripheral OA pain imaging and imaging-guided photothermal treatment in a DMM-induced posttraumatic OA mouse model. Our NGF monoclonal antibody-conjugated nanoprobe (anti-NGF-MoS<sub>2</sub>-AuNR) showed its active targeting capability on the OA knee joint compared to the contralateral intact knee joint under PA imaging *in vivo*. Our results further demonstrated that the increased PA signal intensity in the OA knee was evidenced by histopathological findings of neurovascular invasion in arthritic joint synovial tissues and correlated with the severity of mechanical allodynia in our DMM model. Last

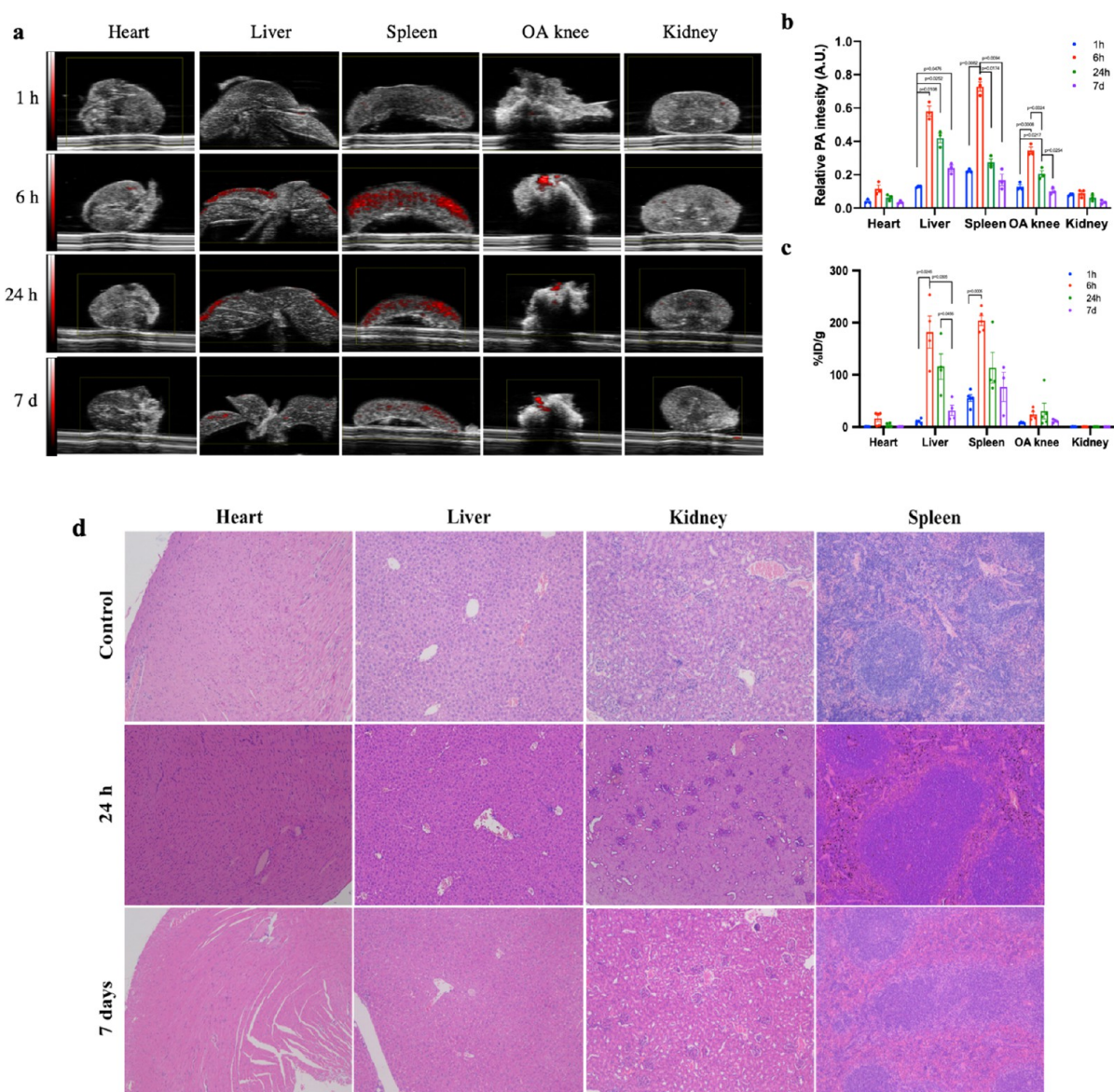


**Figure 3.** Biodistribution and toxicity assessment of vital organs after anti-NGF-MoS<sub>2</sub>-AuNR injection. (a) US-PA overlay images showing signals at 710 nm of *ex vivo* organs and tissues (heart, liver, spleen, OA knee, and kidney) at 1 h, 6 h, 24 h, and 7 days post-i.v. injection of anti-NGF-MoS<sub>2</sub>-AuNR ( $n = 3$  each group). (b) Semiquantitative biodistribution of anti-NGF-MoS<sub>2</sub>-AuNR in mice determined by the average PA intensity of major organs. (c) ICP-MS analysis reflecting the amount of gold element in anti-NGF-MoS<sub>2</sub>-AuNR in the excised tissues. A single intravenous injection of 3.5 mg/kg anti-NGF-MoS<sub>2</sub>-AuNR was given to the mice 1 month after surgery ( $n = 20$ , 5 per group). Organs and knee joints were collected 1 h, 6 h, 24 h, or 7 days after injection. (d) Representative H&E staining of heart, liver, kidney, and spleen 24 h and 7 days after nanoprobe intravenous injection. Statistical analyses were performed using ordinary one-way ANOVA with Tukey's *posthoc* test.

but not least, anti-NGF-MoS<sub>2</sub>-AuNR-mediated photothermal therapy displayed significant pain relief in both the subacute and chronic phase of OA.

## RESULTS AND DISCUSSION

**Design and Synthesis of NGF-Targeted Theranostic Nanoprobes.** Neurovascular invasion with joint destruction contributes to peripheral pain sensations in OA (Figure 1a). The binding of nerve growth factor on TrkA could lead to pain sensations.<sup>43</sup> To prevent NGF binding to TrkA in peripheral pain sensations, we purposely designed a functionalized gold nanorod coated with MoS<sub>2</sub> and then conjugated it with anti-NGF antibody (anti-NGF-MoS<sub>2</sub>-AuNR) (Figure 1b). As

shown *via* high-resolution transmission electron microscopy, we successfully synthesized MoS<sub>2</sub>-AuNR with a MoS<sub>2</sub> coating layer on the surface of the AuNR (aspect ratio of 2.5, length = 50 nm, width = 20 nm) (Figure 1c). The overlapping of Mo and S elements with Au element in TEM elemental images indicated the formation of a MoS<sub>2</sub> layer on the surface of the AuNR (Figure 1c). Differences in surface charges between the AuNR, MoS<sub>2</sub>-AuNR, and anti-NGF-MoS<sub>2</sub>-AuNR were confirmed by changes in zeta-potential, suggesting the successful formation of the conjugate (Figure 1d). The chemical properties of MoS<sub>2</sub>-AuNR have also been further characterized *via* Raman spectroscopy and X-ray diffraction analysis (Figures 1e and S1, Supporting Information). In Raman spectroscopy,

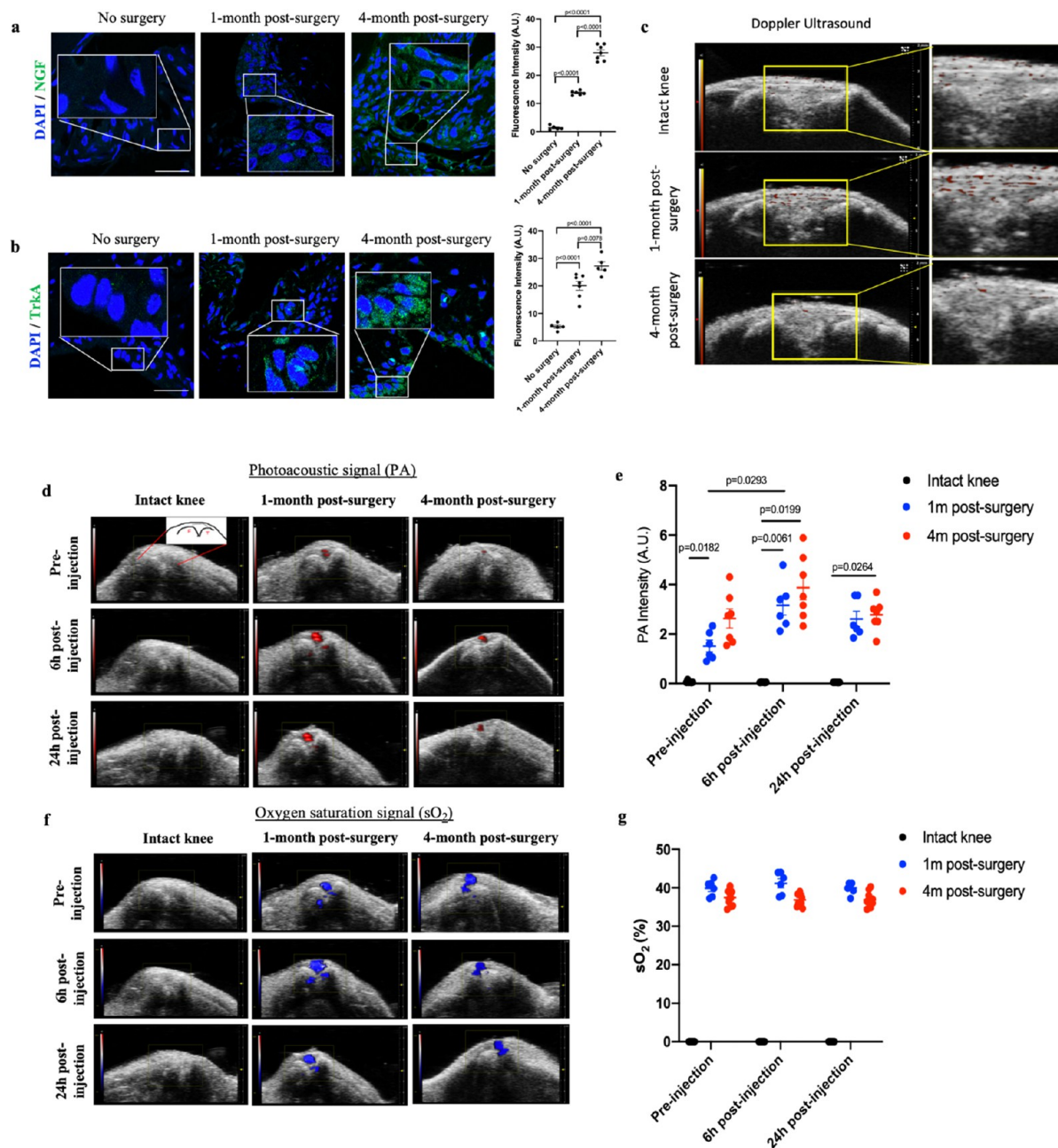


**Figure 4.** Targeting effect of anti-NGF-MoS<sub>2</sub>-AuNR on the OA knee. (a) NGF (green) and (b) TrkA (green) expression were analyzed by immunofluorescence staining together with quantification data. DAPI was used for nuclear counterstaining. Inset magnifications show a close-up view of synoviocytes in the synovium. Scale bars, 25  $\mu\text{m}$  ( $n = 6, 7$  independent biological samples for each group). (c) Images of functional synovial vessels by power Doppler (PD) ultrasonography. PD signals (red) reflect the flow rate of blood in blood vessels. Respective magnified images are shown on the right ( $n = 6, 7$ ). (d) Representative *in vivo* US-PA overlay images of intact knees and surgery knees from mice 1 month ( $n = 6$ ) and 4 months ( $n = 10$ ) after surgery at different time points. (e) Quantitative PA intensities from (d) are shown with mean  $\pm$  SEM. Each data point represents the signal from one knee. (f) Representative US-PA overlay images showing oxygen saturation at a wavelength of 750/850 nm in synovial blood before and after injection in intact and OA knees. (g) PA intensities from (f) are shown with mean  $\pm$  SEM, with each data point representing the signal from one knee. Statistical analyses were performed using ordinary one-way ANOVA with Tukey's *posthoc* test or the Kruskal-Wallis test with Dunn's multiple comparison test (non-normal distribution), when deemed appropriate.

MoS<sub>2</sub> showed characterization peaks at 380 and 402  $\text{cm}^{-1}$  as the E<sub>2g</sub><sup>1</sup> and A<sub>1g</sub> vibration modes, respectively. After interaction with AuNRs, the A<sub>1g</sub> peak of MoS<sub>2</sub> showed a red-shift of 1.86  $\text{cm}^{-1}$ , and an increase of the A<sub>1g</sub>/E<sub>2g</sub><sup>1</sup> peak ratio was also observed due to the interaction between the MoS<sub>2</sub> layer and AuNRs. In addition to the physical and chemical properties, we

examined the binding affinity of our anti-NGF-MoS<sub>2</sub>-AuNR nanocomplex by ELISA (Figure 1f). The binding of the anti-NGF-MoS<sub>2</sub>-AuNR complex was significantly enhanced with the increasing concentration of NGF (Figure 1g).

**Enhanced Biocompatibility and Imaging Performance of MoS<sub>2</sub>-AuNR.** High optical absorbance and high

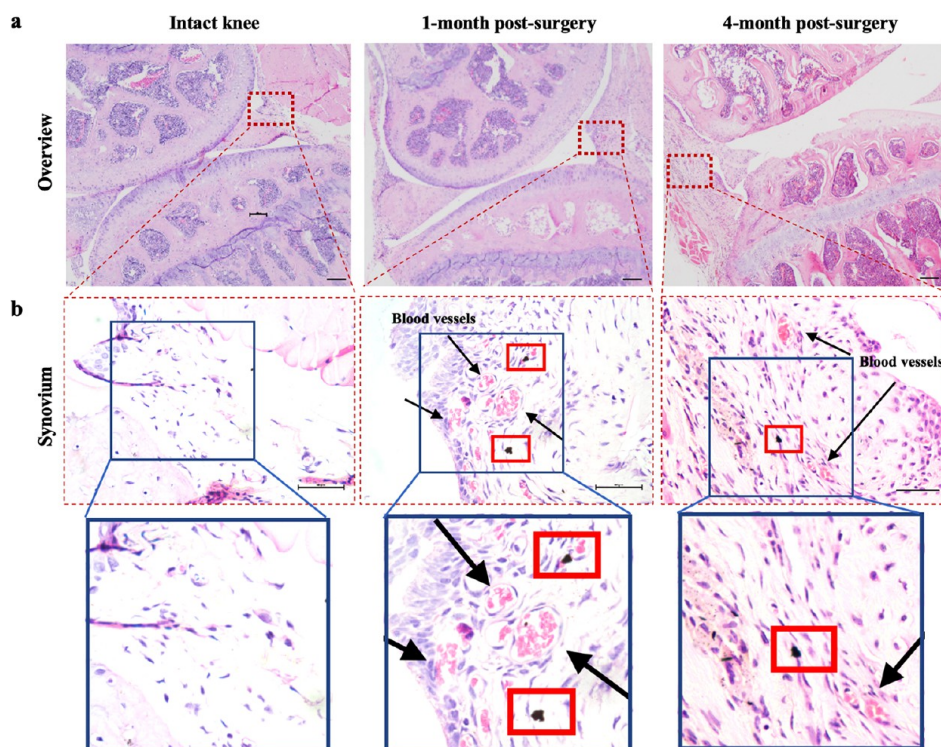


**Figure 5.** Histology of knee joints indicating the targeting effects. (a) Bright-field images of  $5\ \mu\text{m}$  slices of knee joints from control and OA mice stained with hematoxylin and eosin (H&E). (b) Enlarged images of the synovium shown in dotted rectangles of the (a) overview images. Black arrows indicate the presence of blood vessels. Scale bars, (a)  $100\ \mu\text{m}$ ; (b)  $50\ \mu\text{m}$ .

photothermal conversion efficiency of contrast agents in the NIR region are required to promote strong thermal expansion and to generate an enhanced PA signal.<sup>29</sup> Higher characteristic optical absorption peaks at 710 and 510 nm were achieved by coating MoS<sub>2</sub> on AuNRs (Figure S2, Supporting Information), while an enhanced temperature under radiation was recorded in MoS<sub>2</sub>-AuNR when compared to AuNRs or MoS<sub>2</sub> alone (Figure S3, Supporting Information). MoS<sub>2</sub>-AuNR exhibits photothermal capabilities in a concentration- and power density-dependent manner (Figures 2a and S4, Supporting Information), as well as in repeated heating and cooling cycles (Figure 2b). The photothermal conversion efficiency of MoS<sub>2</sub>-AuNR was estimated at around 74.6% on average according to the photothermal heating/dissipation cycle (Figure S5, Supporting Information).

PA imaging performance of MoS<sub>2</sub>-AuNR was further investigated using a setup as shown in Figure S6 (Supporting Information). Finite element simulation showed a 4-fold increase in PA signals in MoS<sub>2</sub>-AuNR compared with AuNRs with a temporal laser pulse (Figure S7, Supporting Information). This is further confirmed in the wavelength of the spectrum, with 4-fold higher PA amplitude in MoS<sub>2</sub>-AuNR than AuNRs at 710 nm (Figure 2c). Moreover, the PA signal intensity of MoS<sub>2</sub>-AuNR also increased in a dose-dependent manner from 50 to 400  $\mu\text{g}/\text{mL}$  (Figures 2d and S8, Supporting Information). Stability in morphology and PA intensities after long-term irradiation (710 nm, 20 Hz, 20  $\text{mJ}/\text{cm}^2$ , <10 ns pulse width) for 30 min makes MoS<sub>2</sub>-AuNR a good candidate for longitudinal imaging (Figure S9, Supporting Information). Cellular uptake and hemolytic potential of this nanocomplex were evaluated before intravenous injection. Coated by a biocompatible MoS<sub>2</sub> layer, MoS<sub>2</sub>-AuNR demonstrated lower

cytotoxicity compared to AuNRs alone (Figure S10, Supporting Information). Strong TPEF signals were observed on MCF-7 cells incubated with a high concentration of 80  $\mu\text{g}/\text{mL}$  MoS<sub>2</sub>-AuNR for up to 24 h without causing any morphological alterations and cell damage (Figure S11, Supporting Information). The hemolysis assay results also showed negligible hemolysis (<5%) of red blood cells upon AuNR, MoS<sub>2</sub>, or MoS<sub>2</sub>-AuNR treatment from 0 to 200  $\mu\text{g}/\text{mL}$ , indicating excellent hemocompatibility of these nanoparticles (Figure 2e). We then examined the *in vivo* PA imaging performance of MoS<sub>2</sub>-AuNR in 4–6-month-old Balb/c mice. AuNR and MoS<sub>2</sub>-AuNR solutions were mixed with Matrigel matrix (v/v = 1:1, the final concentration of Au was 75  $\mu\text{g}/\text{mL}$ ) and subcutaneously injected into the back of a mouse to generate tissue-mimicking phantoms for *in vivo* PA evaluation (Figure 2f). Pure Matrigel matrix was used as a control. As shown in US–PA overlay images, the signal intensity of MoS<sub>2</sub>-AuNR was 2-fold stronger than bare AuNRs at 710 nm for *in vivo* imaging (Figure 2g,h).

We then investigated the biodistribution of MoS<sub>2</sub>-AuNR by measuring the PA signal intensity of major organs such as the heart, liver, kidney, and spleen *ex vivo* after intravenous injection of MoS<sub>2</sub>-AuNR at a dose of 3.5  $\text{mg}/\text{kg}$  in 4–6-month-old female mice. The representative PA images of major organs at different time points are shown in Figure 2i. We observed that MoS<sub>2</sub>-AuNR accumulation reached a maximum in most organs in the initial 6 h, especially in the liver and spleen, and particles were mostly cleared out from the major organs after 7 days (Figure 2j). This finding was further supported by the inductively coupled plasma mass spectrometry (ICP-MS) analysis (Figure 2k).

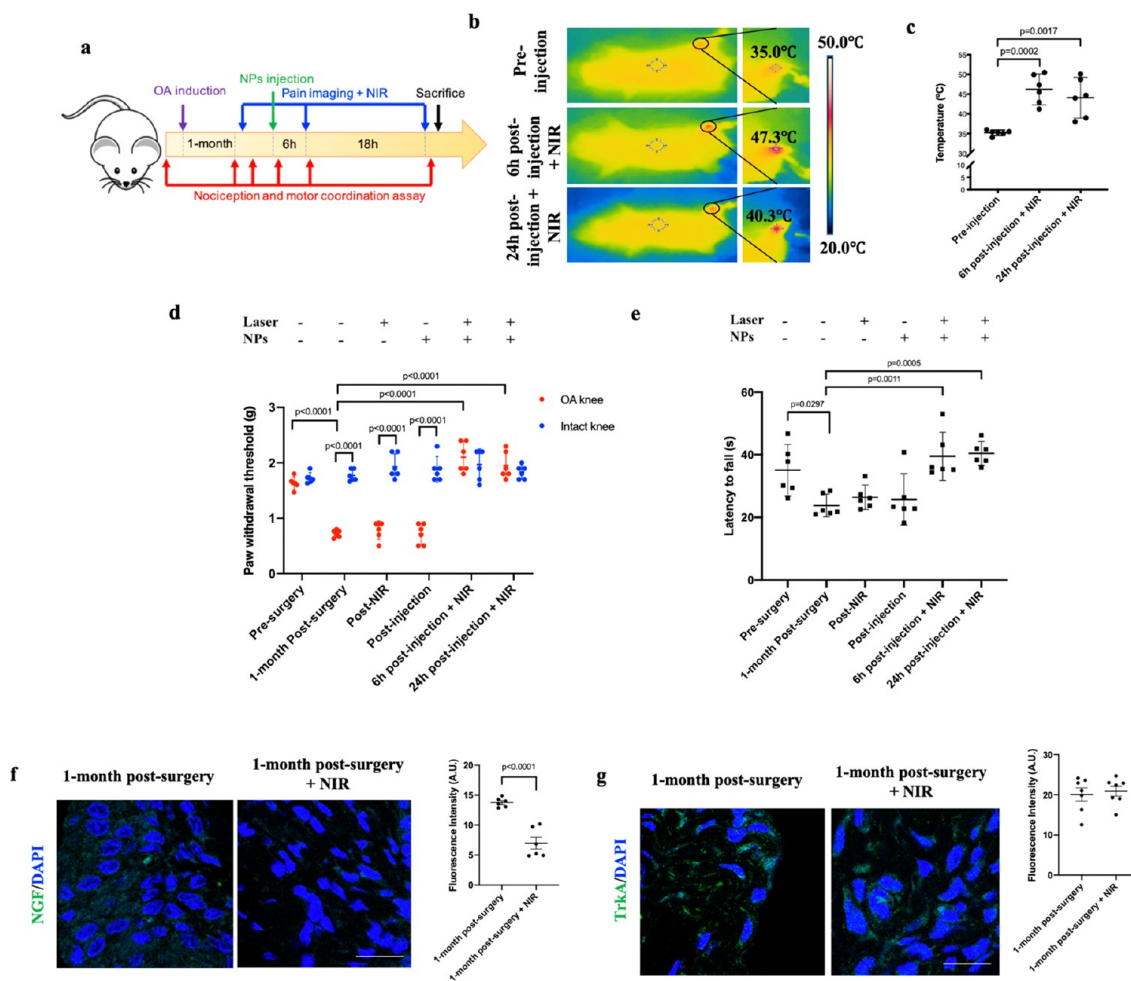


**Figure 6.** Therapeutic effect of nanoprobe-guided laser treatment in early OA. (a) Schematic diagram of the experimental design to investigate the effect of the photothermal therapy on early OA ( $n = 6$ ). (b) IR thermographs showing an increase of temperature in OA knees after intravenous injection of anti-NGF-MoS<sub>2</sub>-AuNR in 1-month postsurgery mice. The temperature of the knees was measured, and the zoomed-in thermographs are shown on the right. (c) Temperature of the OA knees before and 6 h/24 h after injection. (d) Paw withdrawal threshold in response to mechanical stimuli in intact and OA knees was evaluated by the von Frey filament test 1 month after surgery. (e) Motor coordination of mice 1 month postsurgery was assessed by latency to fall using the rotarod test. (f, g) Representative images and quantification of immunofluorescence staining of (f) NGF and (g) TrkA on the synovium of knee joints 1 month after surgery with and without NIR treatment. Scale bar, 25  $\mu\text{m}$ . Data are shown with mean  $\pm$  SEM. Each data point represents data from one animal. Two-way ANOVA with Sidak's multiple comparisons test was used for statistical analysis.

**Biodistribution of NGF-Targeted Nanoprobes for OA Pain Imaging.** To confirm the successful delivery and active targeting effect of anti-NGF-MoS<sub>2</sub>-AuNR to the inflamed joints, we carried out a time-dependent biodistribution of the nanocomplex after injection. A total of 20 4–6-month-old Balb/c mice were divided randomly into four groups ( $n = 5$ ) and sacrificed at different time points (1 h, 6 h, 24 h, and 7 days) after intravenous injection of 3.5 mg/kg anti-NGF-MoS<sub>2</sub>-AuNR. *Ex vivo* US-PA overlay images of the organs showed accumulation of NPs mainly in the liver, spleen, and OA knee (Figure 3a). PA signals at 710 nm reached a maximum at 6 h postinjection, while the signal diminished after 7 days (Figure 3b). In addition, we also quantified the gold deposition in the organs and inflamed knees using ICP-MS. Consistent with the observation from PA imaging, accumulation of NPs in OA knees reached the highest level 6 h after injection (Figure 3c), suggesting 6 h postinjection of NPs might be the optimal time for NGF-targeting therapy for OA pain relief. Histopathological H&E staining of major

organs showed little difference between the saline control group and the anti-NGF-MoS<sub>2</sub>-AuNR group 24 h or 7 days after injection (Figure 3d). Hence, good biocompatibility of our nanoprobe *in vivo* affirmed its potential to be used in nanotherapy.

**Noninvasive NGF-Targeted Pain Imaging *in Vivo*.** In a well-received surgical DMM-induced posttraumatic OA mouse model, the expression of NGF and its receptor, TrkA, significantly increased in the synovium at 1 month and 4 months postsurgery (Figure 4a,b). Meanwhile, synovial blood flow transiently increased at 1 month postsurgery, as visualized under Doppler sonography, and gradually resolved at 4 months after surgery (Figure 4c). Anti-NGF-MoS<sub>2</sub>-AuNR was then deployed to localize NGF in this OA mouse model. Upon intravenous injection, our nanoprobes accumulated and could be visualized in the synovium of OA joints 1 and 4 months after surgery under PA imaging at 710 nm (Figure 4d). No signal could be detected in unoperated intact knees, showing NPs only accumulate at the inflamed regions, which are rich in

NGF (Figure 4d,e). To differentiate between the true signal given by the nanoprobe and the signal from the hemoglobins, which give information about oxygen saturation ( $sO_2$ ) at 750/850 nm, we performed PA analysis at both 710 and 750/850 nm.<sup>36</sup> Our PA imaging result showed  $sO_2$  remains almost at the same level in the OA knee before and after NP injection (Figure 4f,g). This suggests that the difference in PA signal observed at 710 nm before and after surgery was not caused by the changes in surgery-induced  $sO_2$  increase. The conjugated anti-NGF can actively target the inflammatory tissues in the OA joint.

Besides the increase of PA signals, the histology of the knee joints also suggested both a passive and active targeting effect of anti-NGF-MoS<sub>2</sub>-AuNR in the OA synovium. Hematoxylin and eosin (H&E) staining showed synovial membrane angiogenesis and degradation of articular cartilage in OA joints 1 month and 4 months after DMM surgery, respectively. We observed an increase in the number of blood vessels (as indicated by black arrows) in the synovium 1 month after surgery, while the number decreased in late OA (4 months after surgery) (Figure 5a,b), which aligns well with the PA intensity. The increase in permeability of the vessels as demonstrated by power Doppler imaging (Figure 4c) facilitates the passive movement of nanoparticles from the vessels to the synovium by the enhanced permeability and retention (EPR) effect. The EPR effect of nanoprobe has been used for targeting inflamed tissues as a result of deregulated angiogenesis.<sup>44</sup> Nanoparticles (indicated by red rectangles) were observed near blood vessels, showing accumulation of NPs in inflamed tissues rich in NGF (Figure 5b). Moreover, no fibrosis or damaged tissues were observed in surrounding normal tissues, demonstrating the good targeting effect of NIR laser treatment on NGF-positive tissues, and the heat from the laser did not cause any adverse effect to other soft tissues at the joint (Figure 5b). MicroCT analysis of OA knees after injection of nanoparticles further confirms no structural change to the bone (Figure S12, Supporting Information).

**Analgesic Effect of NGF-Targeted Therapy in Early OA.** To determine the optimal concentration of MoS<sub>2</sub>-AuNR intravenously injected into animals, a concentration screening test was performed. Our results indicated that a concentration over 7.0 mg/kg would cause more than 5% hemolysis (Figure S13, Supporting Information). We further measured the temperature of OA knees with NIR irradiation in mice injected with 1.75, 3.5, and 7 mg/kg. A low concentration of 1.75 mg/kg could not generate a satisfactory thermal treatment effect, while the middle and high dose provided a similar increase in local temperature (Figure S14, Supporting Information). Therefore, the optimal concentration we used for the *in vivo* experiment was 3.5 mg/kg. We successfully demonstrated the analgesic effect of our NGF-targeted photothermal therapy in an early OA mouse model. Longitudinal nociception and motor coordination of the animals were monitored before and after surgery and NIR laser treatment (Figure 6a). Unoperated contralateral knees were used as the control for the OA knees. IR thermographs showed an increase in temperature on OA knees after injection of nanoprobe upon irradiation by an 808 nm laser with an output power of 0.2 W/cm<sup>2</sup> for 10 min (Figure 6b,c), while there was no obvious temperature change on intact knees. This again confirms the targeting effect on inflamed tissues of our anti-NGF-MoS<sub>2</sub>-AuNR nanoprobe. To evaluate the long-term retention capability of our nanoprobe in the OA knee, the

temperature on the OA knees after 10 min of laser treatment was measured at different time points for 10 days postinjection. The results showed that the relative temperature increase on OA knees after laser treatment peaked at 6 h postinjection, and a slight drop in mean temperature was observed 1 day after injection. The temperature increase remained at a moderately high level even 2 days after injection, then gradually decreased back to zero (Figure S15, Supporting Information). This suggests the probes were completely cleared out and could not provide a photothermal effect to the inflamed joint 10 days after injection. We assessed the nociceptive tolerance of the animals on both the intact and OA legs before and after NIR laser therapy. Surgery-induced hypersensitivity was observed in OA legs as shown by a large reduction in paw withdrawal threshold in a von Frey test. The threshold remained low until we intravenously injected our nanoprobe and performed NIR therapy on the knee joints. Improvement in pain sensitization was reflected by an increase in paw withdrawal threshold in OA limbs upon laser treatment at 6 and 24 h postinjection (Figure 6d), showing successful pain relief on our OA mouse model. In addition to pain relief, we also showed an improvement in motor balance of OA mice after NGF-targeted photothermal therapy (Figure 6e). In a rotarod test that assesses the motor coordination of the animals, healthy mice could stay a longer time on an accelerating rod compared to OA mice. After treatment, the walking performance of the animals improved significantly 6 and 24 h after injection (Figure 6e). In a long-term efficacy study up to 10 days after injection (Figure S16, Supporting Information), animals performed well 2 days after injection. An analgesic effect resulting from the nanoprobe-based photothermal treatment lasted at least 4 days after injection. Such an effect continued in some animals after 4 days, while it was gradually lost in the other animals until 7 days after injection, when most of the nanoparticles were cleared out (Figure S17a, Supporting Information). A similar trend was also found in the von Frey test, for which the treatment effect could last for at least 4 days and the beneficial effect was lost only after 7 days postinjection (Figure S17b, Supporting Information). The long-lasting pain relief effect of our nanoprobe was superior to indomethacin, a nonsteroidal anti-inflammatory drug (NSAID). Here, indomethacin was administered once intraperitoneally (2.5 mg/kg) in comparison with the nanoprobe treatment group up to 7 days after injection. The indomethacin treatment group could improve motor balance and nociceptive tolerance at 6 h postinjection, and then it quickly lost its therapeutic effect 24 h after injection. Comparatively, the nanoprobe treatment group obviously had a stronger and longer therapeutic effect of at least 4 days (Figure S18, Supporting Information). Since the anti-NGF antibody is an anti-inflammatory agent itself,<sup>45,46</sup> our therapy approach is a combination of an anti-inflammatory agent and photothermal treatment. These results demonstrated the long-lasting therapeutic effect of our active-targeting nanoprobe on OA knees. Expression of NGF decreased in the OA synovium after NIR therapy, while there was no significant change in TrkA expression (Figure 6f,g). This imaging-guided nanotherapy successfully reduced the level of pain by preventing NGF from binding to its receptor without damaging TrkA, therefore blocking the pain response pathway. It further confirmed the targeting effect of our nanoprobe on NGF-expressing tissues.

**Analgesic Effect of NGF-Targeted Therapy in Advanced OA.** To investigate the effect of the nanotherapy in

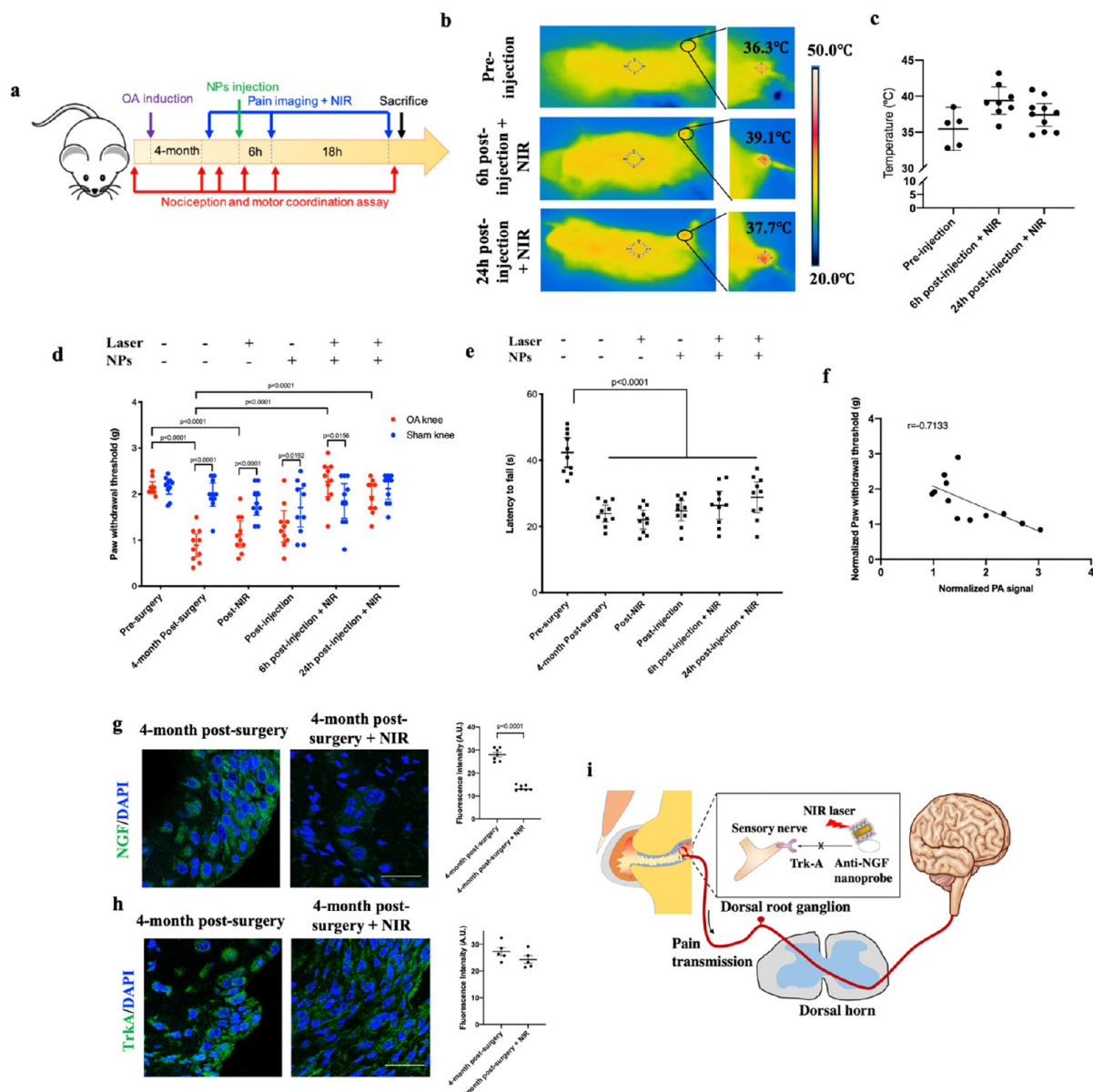


**Figure 7.** Therapeutic effect of nanoprobe-guided laser treatment in late OA. (a) Schematic diagram of the experimental design to investigate the effect of the photothermal therapy on late OA ( $n = 10$ ). (b) Thermographs of OA knees 6 h after anti-NGF-MoS<sub>2</sub>-AuNR injection in 4-month postsurgery mice. The temperature of the knees was measured, and the zoomed-in thermographs are shown on the right. (c) Temperature of the OA knees before and 6 h/24 h after injection. (d) Paw withdrawal thresholds in response to mechanical stimuli in sham and OA knees were evaluated by the von Frey filament test 4 months after surgery. (e) Motor coordination of mice 4 months after DMM surgery assessed by latency to fall using the rotarod test. (f) A negative correlation ( $r = -0.7133$ ) was observed between normalized paw withdrawal threshold and normalized PA signal ( $n = 12$  pairs) of mice 6 h postinjection 1 and 4 months postsurgery. Spearman's correlation coefficient  $r$  is shown on the graph. (g, h) Representative images and quantification of immunofluorescence staining of (g) NGF and (h) TrkA on the synovium of knee joints 4 months after surgery with and without NIR treatment. Scale bar, 25  $\mu$ m. (i) Schematic diagram showing that a NIR laser stops the binding of NGF to TrkA receptors, preventing transmission of pain signals from the periphery to the spinal cord and brain. Data are shown with mean  $\pm$  SEM. Each data point represents data from one animal. Two-way ANOVA with Sidak's multiple comparisons test was used for statistical analysis.

advanced OA, we again examined the changes in tactile sensitivity and motor coordination of the animals 4 months after surgery (Figure 7a). Similarly, the temperature of OA knee joints increased more than the contralateral sham-operated knees and reached a peak at 6 h postinjection (Figure 7b). A lower degree of vascularization (Figure 4f) with lower Doppler signal measured in Doppler ultrasonography (Figure 4c) in more severe OA may cause a smaller difference in

temperature recorded before and after injection of nanoprobe in OA knees compared to that in early OA knees (Figure 7b,c). Similar to the observation in early OA, laser treatment after injection of anti-NGF-MoS<sub>2</sub>-AuNR also reversed the hypersensitivity in advanced OA (Figure 7d). However, it could not improve the motor coordination of mice 4 months after surgery (Figure 7e). By normalizing the PA intensity and paw withdrawal threshold 6 h after nanoprobe injection and NIR

therapy in both early and late OA, we observed a strong negative correlation ( $r = -0.7133$ ) between them (Figure 7f). This showed an accumulation of NGF when the mice experienced a more painful feeling, allowing visualization of nociception in animals. Again, we observed a significant reduction of NGF expression while no obvious decrease of TrkA after photothermal therapy (Figure 7g,h). The proposed pain relief mechanism of our theranostic approach is shown in Figure 7i. The OA pain activation and sensation originate from the upregulation of NGF and its binding to the receptor TrkA on the peripheral sensory nerve. Once anti-NGF-MoS<sub>2</sub>-AuNR nanoprobe target NGF, NIR-based photothermal local treatment will prevent the binding of NGF to TrkA and then block the firing of downstream pain signaling pathways in the dorsal root ganglion, achieving pain relief effects.

## CONCLUSION

In short, we developed an imaging-guided nanoparticle-based theranostic approach for OA pain. The surface coating of MoS<sub>2</sub> on AuNRs could simultaneously enhance the photothermal conversion efficiency and reduce the gold/water interfacial thermal resistance, thus leading to a significantly higher PA imaging signal with enhanced photothermal stability compared to bare AuNRs. Combination of NGF antibody with our MoS<sub>2</sub>-AuNR nanoprobe enables both active and passive targeting on peripheral OA pain generation for targeted NIR treatment. Our results showed targeted photothermal treatment achieved satisfactory pain relief and improvement of motor function in a well-received posttraumatic OA mouse model. This theranostic platform not only allows us to visualize and quantify OA pain but also to mitigate it in a sustainable manner. It warrants further investigations toward clinical application. It holds good promise for clinical translation to achieve long-lasting pain relief by days superior to the up-to-date pain medications by hours, such as indomethacin and NGF antibody, without causing any systemic side-effects and local structural damage.

## METHODS

**Preparation of Molybdenum Disulfide-Modified Gold Nanosheets (MoS<sub>2</sub>-AuNR).** To obtain small-sized MoS<sub>2</sub> nanosheets, a MoS<sub>2</sub> solution (2 mg/mL) was sonicated in an ice bath for 4 h and then centrifuged at 8000 rpm for 15 min. The obtained supernatant was filtered through a 0.22 μm microporous membrane and stored at 4 °C for further usage. Next, MoS<sub>2</sub>-modified AuNRs were prepared by electrostatic interaction between positively charged AuNRs and negatively charged MoS<sub>2</sub>. A AuNR solution (600 μg/mL) was slowly added dropwise to a MoS<sub>2</sub> solution (1:1, v/v) with gentle stirring. After incubating at room temperature overnight, the sample was centrifuged at 6000 rpm for 15 min to separate unbound MoS<sub>2</sub> nanosheets in the supernatant. The obtained precipitate was redispersed in deionized water and stored at 4 °C for further usage.

**Preparation of Anti-NGF Monoclonal Antibody-Conjugated MoS<sub>2</sub>-AuNR (Anti-NGF-MoS<sub>2</sub>-AuNR).** A 5 μL amount of anti-NGF mAbs solution (100 μg/mL) was added into a MoS<sub>2</sub>-AuNR solution and incubated overnight at 4 °C to produce anti-NGF mAbs-MoS<sub>2</sub>-AuNR bioconjugates. The mAbs could bind to MoS<sub>2</sub>-AuNR *via* covalent interaction between MoS<sub>2</sub> nanosheets with sulfur vacancies and free sulfhydryl groups of the antibody.<sup>47</sup> The obtained mixture was purified at 6000 rpm for 10 min and then resuspended in phosphate-buffered saline (PBS) for further usage.

**Measurement of the *in Vitro* Photothermal Effect.** To study the concentration- and time-dependent photothermal effects, MoS<sub>2</sub>-AuNRs at different concentrations (10, 25, 50, 100, and 200 μg/mL, 200 μL) were suspended in centrifuge tubes and irradiated by an 808

nm laser at an output power of 0.2 W cm<sup>-2</sup> for 10 min, respectively. During the irradiation, the temperature of the solutions was recorded every 100 s and the IR thermographs were collected at the end (600 s) using an FLIR C2 infrared camera. In the same manner, the time-dependent photothermal properties of AuNR and MoS<sub>2</sub> (at the same concentration of 200 μg/mL) were studied under an 808 nm laser (0.2 W/cm<sup>2</sup>, 10 min), respectively. The power density- and time-dependent photothermal properties of MoS<sub>2</sub>-AuNRs (200 μg/mL) were investigated with different power densities ranging from 0.02 to 0.2 W/cm<sup>2</sup>.

***In Vivo* Evaluation of MoS<sub>2</sub>-AuNR Photoacoustic Performance by Subcutaneous Injection.** The use of animals in this study was conducted according to the requirements of the Cap. 340 Animal (Control of Experiments) Ordinance and Regulations in Hong Kong. All the animal experiments were approved by the Animal Subjects Ethics Sub-Committee (ASESC). To analyze the PA contrast performance *in vivo*, AuNRs and MoS<sub>2</sub>-AuNRs at the same concentrations of gold (150 μg/mL) were respectively mixed with Matrigel (BD Bioscience, CA, USA) at 1:1 (v/v) ratio in an ice bath. Each mixture (total volume of 100 μL, final concentration of AuNR was 75 μg/mL) was then subcutaneously injected into the back of 12-week-old female Balb/C mice ( $n = 3$ ). Subcutaneous injection of Matrigel alone was used as the control group. After the injection, the tissue-mimicking phantom was successfully generated due to the fast solidification of the Matrigel when the temperature increased. All the samples were imaged simultaneously by the ultrasound microimaging system under 710 nm excitation. The laser condition and parameters of PA measurements were the same as in the *in vitro* evaluation. The data of each sample were collected with the same area of the regions of interest (ROIs) in PA images (1.66 mm<sup>2</sup>) to ensure a fair assessment of *in vivo* results.

***In Vitro* Binding Affinity Test of the Anti-NGF-MoS<sub>2</sub>-AuNR Complex.** The biological affinity of the anti-NGF mAbs-conjugated MoS<sub>2</sub>-AuNR complex to NGF mAbs was evaluated by ELISA. Anti-NGF antibody was first coated in a 96-well plate. A 100 μL amount of NGF (100 ng/mL) was then added to the appropriate wells, incubating for 2.5 h at room temperature with gentle shaking. After rinsing with prepared wash buffer five times, 100 μL of biotinylated anti-NGF mAbs-MoS<sub>2</sub>-AuNR at different concentrations, ranging from 0.05 to 100 ng/mL, was respectively added into each well and incubated for 1 h with gentle shaking. The usages of biotinylated anti-NGF mAbs and MoS<sub>2</sub>-AuNR acted as positive and negative control groups, respectively. After a thorough washing step, streptavidin solution (100 μL) was added to each well and incubated for 45 min at room temperature. Next, 100 μL of TMB one-step substrate reagent was added into each well and incubated for another 30 min in the dark. Lastly, 50 μL of stop solution was added. The absorbance was measured immediately at 450 nm with a microplate reader. Each group had three replicates.

**Animals and DMM Surgery.** The ASESC approved all the experiments listed below (ASESC Case 15-16/17-BME-R-HMRF). Animals were raised at a constant temperature of 25 °C, with a 12/12 light–dark cycle, and supplied with food and water *ad libitum*. To generate a posttraumatic OA model, DMM was performed when the mice reached 4 weeks according to an established protocol.<sup>48</sup> Briefly, the mice were anesthetized by intraperitoneal injection of an anesthetic cocktail [ketamine (100 mg/mL):xylazine (20 mg/mL):saline = 1:0.5:8.5]. Knee joints were opened, and the medial meniscus was cut. No surgery or sham operation was performed on the contralateral knees in the 1-month and 4-month postsurgery group, respectively.

***In Vivo* Experimental Design.** Freshly prepared MoS<sub>2</sub>-Au nanorods conjugated with anti-NGF antibody (anti-NGF-MoS<sub>2</sub>-AuNR) were injected intravenously at 80 μg/mL in the tail at 1 month and 4 months postsurgery. PA imaging was used to delineate the distribution of the nanoparticles *in vivo*. OA knees were exposed to NIR therapy for 10 min under a photothermal camera. NIR treatment was carried out 6 and 24 h after injection of nanoparticles. Von Frey and rotarod tests were performed to assess the locomotive ability and balance of the animals, respectively. Knee joints were

harvested 24 h after injection, and immunohistochemical analysis was carried out.

**High-Frequency Ultrasound, Photoacoustic, and Power Doppler Imaging.** A Vevo2100 high-frequency micro-imaging system (VisualSonics, Toronto, Ontario, Canada) was used for *in vivo* ultrasound, power Doppler, and photoacoustic imaging of the mouse knees according to a previous report.<sup>49</sup> Briefly, the animal was put into general anesthesia by 1–3% isoflurane inhalation. The heart rate and respiratory rate were monitored by attaching the extremities of the animals to electrodes on a heating pad at 37 °C. The legs were flexed to approximately 120°, and the position was fixed using medical tape. Coupling gel was applied to provide a clear visualization of the knee joint. An LZ250 transducer with a broadband frequency of 13–24 MHz was placed parallel to the limb to obtain a sagittal plane of the joint until a triangular region was observed to ensure consistency. The PA signal was measured at 710 nm. The PA acquisition parameters are as follows: frequency: 21 MHz; power: 100%; PA gain: 30 dB; B-mode gain: 18 dB; focus depth: 6 mm; line density: high; persistence: off; sensitivity: high; dynamic range: 65 dB; display map: G5; brightness: 50; contrast: 50. For power Doppler acquisition parameters: frequency: 40 MHz; power: 100%; PRF (pulse repetition frequency): 1 kHz; Doppler gain: 35 dB; 2D gain: 35 dB; focus depth: 4.5 mm; beam angle: 0 deg; sensitivity: 5; line density: full; persistence: low; dynamic range: 60 dB; wall filter: high; priority: 58%. For *ex vivo* organ imaging, the acquisition parameters were similar except the PA gain used was 35 dB. Two hundred frames were captured, and the average PA value was compared between groups. The same area of the ROI for the same animal at different time points was compared.

**Von Frey Filament Test.** Nociceptive sensitization was evaluated by an electronic von Frey anesthesiometer (IITC, USA), allowing detection of force values from 0 to 74 g. A simplified up–down method was used as described by Bonin *et al.*<sup>50</sup> Basically, we started testing at middle filament #3, which corresponds to 1.3 g, after optimization. Up–down rules were applied to select the next filament according to the literature. In brief, the mice were placed on an elevated mesh grid and were allowed to adapt to the environment before measurement. Filaments were applied to the midplantar surface of the OA hind paw and the contralateral paw of the animal when four limbs were resting on the mesh. The force required to cause the withdrawal of the hind paw was recorded after 5 presentations. The exact detected force was recorded by the anesthesiometer. An adjustment factor of  $\pm 0.5$  was added to the final reading from the LCD readout after 5 presentations.

**Rotarod Test.** Motor coordination was assessed by performing a rotarod (Panlab, Harvard Apparatus) test (Movie S1). Mice were placed on the rotating lanes of 5 cm diameter and allowed to walk at a constant speed at 4 rpm for 30 s for adaptation. In this experiment, the rotation was set to accelerate from 4 to 40 rpm over 5 min. Latency to fall (in seconds) and rotation speed of the rod when the animals fell were recorded. Measurements were taken at different time points to assess the endurance and motor coordination of the animals before and after surgery and treatment.

**Laser Treatment and Thermal Imaging of Mouse Knee Joint.** The animal was fixed on a platform with extremities taped, with 1–3% isoflurane inhalation to maintain general anesthesia. An 808 nm laser with an output power of 0.2 W cm<sup>-2</sup> was applied on the knee joints for 10 min. The tip of the laser probe was kept at a 1 cm distance to the irradiated skin, the temperature was measured, and the thermographs were taken immediately after removal of the probe using an FLIR C2 infrared camera.

**Biodistribution by ICP-MS.** Major organs, including the heart, liver, spleen, kidney, and knees, were harvested 1 h, 6 h, 24 h, and 7 days after MoS<sub>2</sub>-AuNR injection and fixed with 10% formalin. The collected organs were then dried, weighed, and digested by trace metal grade nitric acid (69%) solution at 130 °C. After that, all the samples were diluted to 25 mL and filtered through a 0.45  $\mu$ m membrane. Then, ICP-MS was used to quantify the uptake amount of Au in different organs and joint tissues (Agilent 7500ce, Octopole reaction system, USA). Each group had five mice as replicates.

**Histology and Immunohistochemistry.** Samples were harvested at specific time points. Organs and knee joints were fixed in 4% paraformaldehyde (PFA), and joints were decalcified using 10% ethylenediaminetetraacetic acid (EDTA) at pH 7.4. The tissues were then dehydrated in an alcohol gradient and embedded in paraffin. Five-micrometer-thick sections were used for H&E staining for histomorphological evaluation. For immunohistochemistry, the knee sections were incubated with primary antibodies of NGF (ab6199, Abcam) and TrkA (ab216626, Abcam) overnight at 4 °C, followed by visualization by fluorescence-conjugated secondary antibodies or diaminobenzidine. A Leica TCS SPE confocal microscope and a Nikon ECLIPSE 80i were used to capture the images.

**Statistical Analysis.** All data were presented using mean  $\pm$  SEM. For comparison of signal intensities, one-way analysis of variance (ANOVA) or the Kruskal–Wallis test was used when deemed appropriate. Respective *posthoc* tests were carried out when overall significance was detected between groups. For parameters for behavioral tests between different time points, two-way ANOVA with Sidak's multiple comparisons test was used for statistical analysis. The level of significance was set at  $p < 0.05$ . Statistical analysis and graphs were generated using SPSS 23.0 and Graphpad Prism 8.

## ASSOCIATED CONTENT

### Supporting Information

The Supporting Information is available free of charge at <https://pubs.acs.org/doi/10.1021/acsnano.1c02454>.

Purchased materials, material characterization description, X-ray diffraction of MoS<sub>2</sub>-AuNR, UV–vis absorption spectra of MoS<sub>2</sub>-AuNR, photothermal characterization with laser irradiation time and with nanoprobe concentrations, single photothermal heating/cooling cycle of MoS<sub>2</sub>-AuNR, *in vivo* PA imaging experimental setup, simulation of photoacoustic pulse signal of MoS<sub>2</sub>-AuNR, PA performance comparison between AuNR and MoS<sub>2</sub>-AuNR, photothermal stability testing of MoS<sub>2</sub>-AuNR, cytotoxicity and hemocompatibility testing, *in vitro* cellular uptake testing, hemolytic effect of MoS<sub>2</sub>-AuNR doses, infrared thermographs of mouse OA knees with various MoS<sub>2</sub>-AuNR doses, long-term efficacy study design, long-term monitoring of pain and motor balance, comparison between effects of anti-NGF-MoS<sub>2</sub>-AuNR and indomethacin, and an example of a rotarod experiment (PDF)

Movie showing the rotarod test (MP4)

## AUTHOR INFORMATION

### Corresponding Authors

**Chunyi Wen** – Department of Biomedical Engineering, Faculty of Engineering and Research Institute of Smart Ageing, The Hong Kong Polytechnic University, Hong Kong, China; [orcid.org/0000-0003-1949-7822](https://orcid.org/0000-0003-1949-7822); Email: [chunyi.wen@polyu.edu.hk](mailto:chunyi.wen@polyu.edu.hk)

**Mo Yang** – Department of Biomedical Engineering, Faculty of Engineering, The Hong Kong Polytechnic University, Hong Kong, China; [orcid.org/0000-0002-3863-8187](https://orcid.org/0000-0002-3863-8187); Email: [mo.yang@polyu.edu.hk](mailto:mo.yang@polyu.edu.hk)

### Authors

**Man Ting Au** – Department of Biomedical Engineering, Faculty of Engineering, The Hong Kong Polytechnic University, Hong Kong, China

**Jingyu Shi** – Department of Biomedical Engineering, Faculty of Engineering, The Hong Kong Polytechnic University, Hong Kong, China

Yadi Fan – Department of Biomedical Engineering, Faculty of Engineering, The Hong Kong Polytechnic University, Hong Kong, China

Junguo Ni – Department of Biomedical Engineering, Faculty of Engineering, The Hong Kong Polytechnic University, Hong Kong, China

Complete contact information is available at:  
<https://pubs.acs.org/10.1021/acsnano.1c02454>

### Author Contributions

<sup>§</sup>M.T.A. and J.S. contributed equally.

### Author Contributions

C.Y.W. and M.Y. conceived and designed the experiments with M.T.A. and J.Y.S. M.T.A., J.Y.S., and Y.D.F. performed all experiments in the initial stage, and J.G.N. significantly contributed to the experiments during the revision period. All authors analyzed and discussed the data. M.T.A., J.Y.S., J.G.N., M.Y., and C.Y.W. wrote and revised the paper.

### Notes

The authors declare no competing financial interest.

### ACKNOWLEDGMENTS

This work was supported by Health and Medical Research Fund Scheme (01150087, 16172691), Research Grants Council of Hong Kong ECS (PolyU 251008/18M), GRF (PolyU 151061/20M and 152169/17E), NFSC/RGC schemes (N\_PolyU520/20), the National Natural Science Foundation of China (NSFC) (Grant No. 31771077), and the Hong Kong Polytechnic University Project of Strategic Importance (ZE1E, ZE2C). The authors also thank the University Research Facility in Life Sciences (ULS) for providing equipment and technical support.

### REFERENCES

- (1) Puig-Junoy, J.; Ruiz Zamora, A. Socio-Economic Costs of Osteoarthritis: A Systematic Review of Cost-of-Illness Studies. *Semin. Arthritis Rheum.* **2015**, *44* (5), 531–541.
- (2) Malfait, A. M.; Schnitzer, T. J. Towards a Mechanism-Based Approach to Pain Management in Osteoarthritis. *Nat. Rev. Rheumatol.* **2013**, *9* (11), 654–64.
- (3) Hawker, G. A.; Stewart, L.; French, M. R.; Cibere, J.; Jordan, J. M.; March, L.; Suarez-Almazor, M.; Gooberman-Hill, R. Understanding the Pain Experience in Hip and Knee Osteoarthritis—An OARSI/OMERACT Initiative. *Osteoarthr. Cartil.* **2008**, *16* (4), 415–22.
- (4) Dieppe, P. A.; Lohmander, L. S. Pathogenesis and Management of Pain in Osteoarthritis. *Lancet* **2005**, *365* (9463), 965–73.
- (5) Yue, Y.; Collaku, A. Correlation of Pain Reduction with fMRI BOLD Response in Osteoarthritis Patients Treated with Paracetamol: Randomized, Double-Blind, Crossover Clinical Efficacy Study. *Pain Med.* **2018**, *19* (2), 355–367.
- (6) Keszthelyi, D.; Aziz, Q.; Ruffle, J. K.; O'Daly, O.; Sanders, D.; Krause, K.; Williams, S. C. R.; Howard, M. A. Delineation between Different Components of Chronic Pain Using Dimension Reduction - An ASL fMRI Study in Hand Osteoarthritis. *Eur. J. Pain* **2018**, *22* (7), 1245–1254.
- (7) Valdes, A. M.; Doherty, S. A.; Zhang, W.; Muir, K. R.; Maciewicz, R. A.; Doherty, M. Inverse Relationship between Preoperative Radiographic Severity and Postoperative Pain in Patients with Osteoarthritis Who Have Undergone Total Joint Arthroplasty. *Semin. Arthritis Rheum.* **2012**, *41* (4), 568–75.
- (8) Hofmann, S.; Seitlinger, G.; Djahani, O.; Pietsch, M. The Painful Knee after TKA: A Diagnostic Algorithm for Failure Analysis. *Knee Surg. Sports Traumatol. Arthrosc.* **2011**, *19* (9), 1442–52.
- (9) Vargas, E. S. N. C. O.; Dos Anjos, R. L.; Santana, M. M. C.; Battistella, L. R.; Marcon Alfieri, F. Discordance between Radiographic Findings, Pain, and Superficial Temperature in Knee Osteoarthritis. *Reumatologia* **2020**, *58* (6), 375–380.
- (10) Bedson, J.; Croft, P. R. The Discordance between Clinical and Radiographic Knee Osteoarthritis: A Systematic Search and Summary of the Literature. *BMC Musculoskeletal Disord.* **2008**, *9*, DOI: 10.1186/1471-2474-9-116.
- (11) Vincent, T. L. Peripheral Pain Mechanisms in Osteoarthritis. *Pain* **2020**, *161*, S138–S146.
- (12) Miller, R. E.; Tran, P. B.; Obeidat, A. M.; Raghu, P.; Ishihara, S.; Miller, R. J.; Malfait, A. M. The Role of Peripheral Nociceptive Neurons in the Pathophysiology of Osteoarthritis Pain. *Curr. Osteoporos. Rep.* **2015**, *13* (5), 318–26.
- (13) Aloe, L.; Rocco, M. L.; Balzamino, B. O.; Micera, A. Nerve Growth Factor: Role in Growth, Differentiation and Controlling Cancer Cell Development. *J. Exp. Clin. Cancer Res.* **2016**, *35* (1), 116.
- (14) Aloe, L.; Tuveri, M. A.; Carcassi, U.; Levi-Montalcini, R. Nerve Growth Factor in the Synovial Fluid of Patients with Chronic Arthritis. *Arthritis Rheum.* **1992**, *35* (3), 351–5.
- (15) McNamee, K. E.; Burleigh, A.; Gompels, L. L.; Feldmann, M.; Allen, S. J.; Williams, R. O.; Dawbarn, D.; Vincent, T. L.; Inglis, J. J. Treatment of Murine Osteoarthritis with TrkAd5 Reveals a Pivotal Role for Nerve Growth Factor in Non-Inflammatory Joint Pain. *Pain* **2010**, *149* (2), 386–92.
- (16) Pecchi, E.; Priam, S.; Gosset, M.; Pigenet, A.; Sudre, L.; Laiguillon, M. C.; Berenbaum, F.; Houard, X. Induction of Nerve Growth Factor Expression and Release by Mechanical and Inflammatory Stimuli in Chondrocytes: Possible Involvement in Osteoarthritis Pain. *Arthritis Res. Ther.* **2014**, *16* (1), R16.
- (17) Ashraf, S.; Mapp, P. I.; Burston, J.; Bennett, A. J.; Chapman, V.; Walsh, D. A. Augmented Pain Behavioural Responses to Intra-Articular Injection of Nerve Growth Factor in Two Animal Models of Osteoarthritis. *Ann. Rheum. Dis.* **2014**, *73*, 1710.
- (18) Iannone, F.; De Bari, C.; Dell'Accio, F.; Covelli, M.; Patella, V.; Lo Bianco, G.; Lapadula, G. Increased Expression of Nerve Growth Factor (NGF) and High Affinity NGF Receptor (p140 TrkA) in Human Osteoarthritic Chondrocytes. *Rheumatology (Oxford)* **2002**, *41* (12), 1413–1418.
- (19) Huang, H.; Shank, G.; Ma, L.; Tallents, R. H.; Kyrkanides, S. Nerve Growth Factor Induced after Temporomandibular Joint Inflammation Decelerates Chondrocyte Differentiation. *Oral Dis* **2013**, *19* (6), 604–10.
- (20) Kc, R.; Li, X.; Kroin, J. S.; Liu, Z.; Chen, D.; Xiao, G.; Levine, B.; Li, J.; Hamilton, J. L.; van Wijnen, A. J.; Piel, M.; Shelly, D. A.; Brass, D.; Kolb, E.; Im, H. J. PKCdelta Null Mutations in a Mouse Model of Osteoarthritis Alter Osteoarthritic Pain Independently of Joint Pathology by Augmenting NGF/TrkA-Induced Axonal Outgrowth. *Ann. Rheum. Dis.* **2016**, *75* (12), 2133–2141.
- (21) Chuang, H. H.; Prescott, E. D.; Kong, H.; Shields, S.; Jordt, S. E.; Basbaum, A. I.; Chao, M. V.; Julius, D. Bradykinin and Nerve Growth Factor Release the Capsaicin Receptor from PtdIns(4,5)P2-Mediated Inhibition. *Nature* **2001**, *411* (6840), 957–62.
- (22) Ji, R. R.; Samad, T. A.; Jin, S. X.; Schmall, R.; Woolf, C. J. p38 MAPK Activation by NGF in Primary Sensory Neurons after Inflammation Increases TRPV1 Levels and Maintains Heat Hyperalgesia. *Neuron* **2002**, *36* (1), 57–68.
- (23) Schmelz, M.; Mantyh, P.; Malfait, A. M.; Farrar, J.; Yaksh, T.; Tive, L.; Viktrup, L. Nerve Growth Factor Antibody for the Treatment of Osteoarthritis Pain and Chronic Low-Back Pain: Mechanism of Action in the Context of Efficacy and Safety. *Pain* **2019**, *160* (10), 2210–2220.
- (24) Nwosu, L. N.; Mapp, P. I.; Chapman, V.; Walsh, D. A. Blocking the Tropomyosin Receptor Kinase A (TrkA) Receptor Inhibits Pain Behaviour in Two Rat Models of Osteoarthritis. *Ann. Rheum. Dis.* **2016**, *75* (6), 1246–54.
- (25) Lane, N. E.; Schnitzer, T. J.; Birbara, C. A.; Mokhtarani, M.; Shelton, D. L.; Smith, M. D.; Brown, M. T. Tanezumab for the

- Treatment of Pain from Osteoarthritis of the Knee. *N. Engl. J. Med.* **2010**, *363* (16), 1521–31.
- (26) Xiao, S. Y.; Tang, Y. F.; Lin, Y. M.; Lv, Z.; Chen, L. Tracking Osteoarthritis Progress through Cationic Nanoprobe-Enhanced Photoacoustic Imaging of Cartilage. *Acta Biomater.* **2020**, *109*, 153–162.
- (27) Ye, J. M.; Li, Z.; Fu, Q. R.; Li, Q. Q.; Zhang, X.; Su, L. C.; Yang, H. H.; Song, J. B., Quantitative Photoacoustic Diagnosis and Precise Treatment of Inflammation *in Vivo* Using Activatable Theranostic Nanoprobe. *Adv. Funct. Mater.* **2020**, *30* (38), 2001771.
- (28) Xiao, S.; Chen, L. The Emerging Landscape of Nanotheranostic-Based Diagnosis and Therapy for Osteoarthritis. *J. Controlled Release* **2020**, *328*, 817–833.
- (29) Wang, L. V.; Hu, S. Photoacoustic Tomography: *In Vivo* Imaging from Organelles to Organs. *Science* **2012**, *335* (6075), 1458–62.
- (30) Choi, J.; Yang, J.; Jang, E.; Suh, J. S.; Huh, Y. M.; Lee, K.; Haam, S. Gold Nanostructures as Photothermal Therapy Agent for Cancer. *Anti-Cancer Agents Med. Chem.* **2011**, *11* (10), 953–964.
- (31) Li, W. W.; Chen, X. Y. Gold Nanoparticles for Photoacoustic Imaging. *Nanomedicine* **2015**, *10* (2), 299–320.
- (32) Chen, Y. S.; Frey, W.; Kim, S.; Kruizinga, P.; Homan, K.; Emelianov, S. Silica-Coated Gold Nanorods as Photoacoustic Signal Nanoamplifiers. *Nano Lett.* **2011**, *11* (2), 348–354.
- (33) Moon, H.; Kumar, D.; Kim, H.; Sim, C.; Chang, J. H.; Kim, J. M.; Kim, H.; Lim, D. K. Amplified Photoacoustic Performance and Enhanced Photothermal Stability of Reduced Graphene Oxide Coated Gold Nanorods for Sensitive Photo acoustic Imaging. *ACS Nano* **2015**, *9* (3), 2711–2719.
- (34) Tian, F.; Lyu, J.; Shi, J. Y.; Yang, M. Graphene and Graphene-Like Two-Denominational Materials Based Fluorescence Resonance Energy Transfer (FRET) Assays for Biological Applications. *Biosens. Bioelectron.* **2017**, *89*, 123–135.
- (35) Gupta, D.; Chauhan, V.; Kumar, R. A Comprehensive Review on Synthesis and Applications of Molybdenum Disulfide (MoS<sub>2</sub>) Material: Past and Recent Developments. *Inorg. Chem. Commun.* **2020**, *121*, 108200.
- (36) Oudeng, G.; Au, M. T.; Shi, J. Y.; Wen, C. Y.; Yang, M. One-Step *in Situ* Detection of miRNA-21 Expression in Single Cancer Cells Based on Biofunctionalized MoS<sub>2</sub> Nanosheets. *ACS Appl. Mater. Interfaces* **2018**, *10* (1), 350–360.
- (37) Shi, J. Y.; Lyu, J.; Tian, F.; Yang, M. A Fluorescence Turn-On Biosensor Based on Graphene Quantum Dots (GQDs) and Molybdenum Disulfide (MoS<sub>2</sub>) Nanosheets for Epithelial Cell Adhesion Molecule (EpCAM) Detection. *Biosens. Bioelectron.* **2017**, *93*, 182–188.
- (38) Oudeng, G.; Benz, M.; Popova, A. A.; Zhang, Y.; Yi, C. Q.; Levkin, P. A.; Yang, M. Droplet Microarray Based on Nanosensing Probe Patterns for Simultaneous Detection of Multiple HIV Retroviral Nucleic Acids. *ACS Appl. Mater. Interfaces* **2020**, *12* (50), 55614–55623.
- (39) Chou, S. S.; Kaehr, B.; Kim, J.; Foley, B. M.; De, M.; Hopkins, P. E.; Huang, J.; Brinker, C. J.; Dravid, V. P. Chemically Exfoliated MoS<sub>2</sub> as Near-Infrared Photothermal Agents. *Angew. Chem., Int. Ed.* **2013**, *52* (15), 4160–4164.
- (40) Chen, J. Q.; Liu, C. B.; Hu, D. H.; Wang, F.; Wu, H. W.; Gong, X. J.; Liu, X.; Song, L.; Sheng, Z. H.; Zheng, H. R. Single-Layer MoS<sub>2</sub> Nanosheets with Amplified Photoacoustic Effect for Highly Sensitive Photoacoustic Imaging of Orthotopic Brain Tumors. *Adv. Funct. Mater.* **2016**, *26* (47), 8715–8725.
- (41) Wang, S. G.; Li, X.; Chen, Y.; Cai, X. J.; Yao, H. L.; Gao, W.; Zheng, Y. Y.; An, X.; Shi, J. L.; Chen, H. R. A Facile One-Pot Synthesis of a Two-Dimensional MoS<sub>2</sub>/Bi<sub>2</sub>S<sub>3</sub> Composite Theranostic Nanosystem for Multi-Modality Tumor Imaging and Therapy. *Adv. Mater.* **2015**, *27* (17), 2775–2782.
- (42) Yu, J.; Yin, W. Y.; Zheng, X. P.; Tian, G.; Zhang, X.; Bao, T.; Dong, X. H.; Wang, Z. L.; Gu, Z. J.; Ma, X. Y.; Zhao, Y. L. Smart MoS<sub>2</sub>/Fe<sub>3</sub>O<sub>4</sub> Nanotheranostic for Magnetically Targeted Photothermal Therapy Guided by Magnetic Resonance/Photoacoustic Imaging. *Theranostics* **2015**, *5* (9), 931–945.
- (43) Hay, O. Y.; Cohen, M.; Nitzan, I.; Kasirer, Y.; Shahroor-Karni, S.; Yitzhaky, Y.; Engelberg, S.; Nitzan, M. Pulse Oximetry with Two Infrared Wavelengths without Calibration in Extracted Arterial Blood. *Sensors* **2018**, *18* (10), 3457.
- (44) Nehoff, H.; Parayath, N. N.; Domanovitch, L.; Taurin, S.; Greish, K. Nanomedicine for Drug Targeting: Strategies beyond the Enhanced Permeability and Retention Effect. *Int. J. Nanomed.* **2014**, *9*, 2539–2555.
- (45) Xu, L.; Nwosu, L. N.; Burston, J. J.; Millns, P. J.; Sagar, D. R.; Mapp, P. I.; Meesawatsom, P.; Li, L.; Bennett, A. J.; Walsh, D. A.; Chapman, V. The Anti-NGF Antibody MuMab 911 Both Prevents and Reverses Pain Behaviour and Subchondral Osteoclast Numbers in a Rat Model of Osteoarthritis Pain. *Osteoarthritis and Cartilage* **2016**, *24* (9), 1587–1595.
- (46) Seah, K. T. M.; Rammanohar, J.; Sutton, J.; Kendrick, T.; Khan, W. S. The Effectiveness of Anti-Nerve Growth Factor Monoclonal Antibodies in the Management of Pain in Osteoarthritis of the Hip and Knee: A PRISMA Systematic Review and Meta-Analysis. *Pain Med.* **2021**, *22* (5), 1185–1204.
- (47) Nguyen, E. P.; Carey, B. J.; Ou, J. Z.; van Embden, J.; Della Gaspera, E.; Chrimes, A. F.; Spencer, M. J. S.; Zhuyikov, S.; Kalantar-zadeh, K.; Daenke, T. Electronic Tuning of 2D MoS<sub>2</sub> through Surface Functionalization. *Adv. Mater.* **2015**, *27* (40), 6225–6229.
- (48) Glasson, S. S.; Blanchet, T. J.; Morris, E. A. The Surgical Destabilization of the Medial Meniscus (DMM) Model of Osteoarthritis in the 129/SvEv Mouse. *Osteoarthr. Cartil.* **2007**, *15* (9), 1061–1069.
- (49) Liu, Z. Y.; Au, M. T.; Wang, X.; Chan, P. M. B.; Lai, P. X.; Sun, L.; Zheng, Y. P.; Rong, L. M.; Wen, C. Y. Photoacoustic Imaging of Synovial Tissue Hypoxia in Experimental Post-Traumatic Osteoarthritis. *Prog. Biophys. Mol. Biol.* **2019**, *148*, 12–20.
- (50) Bonin, R. P.; Bories, C.; De Koninck, Y. A Simplified Up-Down Method (SUDO) for Measuring Mechanical Nociception in Rodents Using Von Frey Filaments. *Mol. Pain* **2014**, *10*, DOI: 10.1186/1744-8069-10-26.